High precipitation rates characterize biomineralization in the benthic foraminifer *Ammonia beccarii*

Esmee Geerken [a], Lennart de Nooijer [a,*], Takashi Toyofuku [b], Anne Roepert [c,1],
Jack J. Middelburg [c], Michiel V.M. Kienhuis [c], Yukiko Nagai [b], Lubos Polerecky [c],
Gert-Jan Reichart [a,c]

[a] *Department of Ocean Systems, NIOZ-Royal Netherlands Institute for Sea Research, and Utrecht University, Den Burg, the Netherlands*
[b] *Institute for Extra-cutting-edge Science and Technology Avant-garde Research (X-STAR), Japan Agency for Marine-Earth Science and Technology (JAMSTEC), Natsushima-cho 2-15, Yokosuka 237-0061, Japan*
[c] *Department of Earth Sciences, Faculty of Geosciences, Utrecht University, Utrecht, the Netherlands*

Abstract

The chemical composition of foraminiferal calcite reflects seawater variables and is therefore a popular paleoceanographic tool. The sedimentary record of foraminiferal shell chemistry is, however, mostly interpreted using empirical calibrations. Since geochemical patterns in foraminifera often deviate from inorganic analogues, there is an ongoing need for a more mechanistic understanding of foraminiferal biomineralization. One of the most elusive, but potentially important parameters characterizing foraminiferal biomineralization is the rate of calcite precipitation. Using a combination of labelling experiments and sub-micrometer imaging of the incorporated label with NanoSIMS, we show that the benthic foraminifer *Ammonia beccarii* precipitates its calcite at a rate of $\sim 24 \pm 4$ nmol/cm^2/min. These values are close to maximum reported rates for inorganic calcite precipitation from Mg-depleted seawater, which is consistent with the strong fractionation against Mg during biomineralization. At the same time, the measured precipitation rate is in accordance with the similarity between the foraminiferal Sr/Ca values and ratios from calcite precipitated inorganically at these rates. Our results also show that the observed precipitation rate is surprisingly uniform among specimens and within chamber walls, indicating that the small-scale element banding is not reflecting variability in precipitation rate. Based on our results, we present a conceptual model where foraminiferal calcification is characterized by two major processes: first, active ion transport determines the composition of the calcifying fluid, whereas thermodynamics and process kinetics dictate fractionation and partitioning during the subsequent calcium carbonate precipitation. This model also accounts for a role of seawater transport, which may be important in the first steps of calcification to explain geochemical signatures of other foraminiferal taxa.
© 2021 The Author(s). Published by Elsevier Ltd. This is an open access article under the CC BY license (http://creativecommons.org/licenses/by/4.0/).

Keywords: Foraminifera; Calcification; Geochemistry

1. INTRODUCTION

Calcium carbonate is the most widely occurring biomineral on Earth (Knoll, 2003), and its production has a profound impact on global carbon cycling and atmospheric carbon dioxide concentrations (Zeebe and Westbroek, 2003; Ridgwell and Zeebe, 2005). Foraminifera, unicellular

* Corresponding author.
  E-mail address: lennart.de.nooijer@nioz.nl (L. de Nooijer).
[1] Present address: Soil Chemistry and Chemical Soil Quality, Wageningen University, P.O. Box 47, 6700 AA Wageningen, the Netherlands.

marine organisms that first appeared in the fossil record 500 million years ago (Culver, 1991; Pawlowski et al., 2003), secrete calcite shells that in the open ocean currently contribute up to 50% of the calcium carbonate production (Schiebel, 2002). Besides their impact on the global carbon cycle, the chemical composition of fossil specimens is a frequently used tool to reconstruct past environments and climates. This is possible since incorporation of trace elements and fractionation of isotopes during biomineralization depend on environmental conditions, including temperature (Nürnberg et al., 1996; Anand et al., 2003), salinity (Urey et al., 1951; Wit et al., 2013; Geerken et al., 2018), element concentration (Boyle, 1981) and sea water pH (Sanyal et al., 1996). These relationships can be partly explained by kinetic and thermodynamic principles, but also reflect biological control during calcification (Urey et al., 1951; Erez, 2003). Identifying the mechanisms involved in foraminiferal biomineralization is essential for understanding element partitioning between sea water and foraminiferal shell carbonate and hence their application for reconstructing past environments. For most trace elements, concentrations in the calcite shell are relatively low compared to non-biological calcite precipitated from seawater, which has fuelled debate on the mechanisms responsible for transporting ions from seawater into the calcifying space (Elderfield et al., 1996; Erez, 2003; Nehrke et al., 2013; De Nooijer et al., 2014; Toyofuku et al., 2017).

Observations on biomineralizing foraminifera showed the involvement of seawater vacuoles (Erez, 2003), pH-regulation (Bentov et al., 2009; De Nooijer et al., 2009a; Toyofuku et al., 2017), organic templates (Branson et al., 2016), membranes secluding the calcifying fluid from seawater, and complex cytoskeleton arrangements (Tyszka et al., 2019). The latter, for example, is believed to be responsible for providing a delineated space in which new calcite precipitates (Nagai et al., 2018a; 2018b). Together, these processes are suggested to dictate the conditions and element composition of the calcifying fluid from which foraminifera precipitate their calcite. Efforts to integrate these various effects on element incorporation resulted in models including Rayleigh fractionation (Elderfield et al., 1996), specific ion (e.g. Mg^{2+}) removal (Zeebe and Sanyal, 2002) and trans-membrane Ca^{2+}-transport into the calcifying fluid (Nehrke et al., 2013). Although these models partly explain observed sensitivities of element incorporation to environmental parameters, a large unknown with profound impact on foraminiferal shell chemistry is the calcite's precipitation rate, which remains poorly constrained.

The precipitation rate has been shown to impact element partitioning in inorganic calcites, whereby higher rates promote incorporation of Na^+ (Busenberg and Plummer, 1985), B^+ (Mavromatis et al., 2015), Sr^{2+} (Lorens, 1981; Tesoriero and Pankow, 1996), SO_4^{2-} (Busenberg and Plummer, 1985) and Ba^{2+} (Tesoriero and Pankow, 1996), and decrease incorporation of Mg^{2+} (Burton and Walter, 1991), Mn^{2+}, Co^{2+} and Cd^{2+} (Lorens, 1981). Foraminiferal calcite growth rates have been estimated by determining rates of chamber addition (Dueñas-Bohórquez et al.,

2011) and by measuring changes in alkalinity over time (Erez, 2003). These approaches only provide a time-averaged rate and since calcite precipitation by benthic, low Mg/Ca species of foraminifera is episodic rather than continuous (Erez, 2003; Tyszka et al., 2019), lead to an underestimation of crystal growth rates. Quantifying foraminiferal calcite precipitation rates therefore requires analysing fluxes of calcite addition during a single chamber formation event.

Precipitation rate during foraminiferal biomineralization is likely largely controlled by the flux of ions into the calcifying fluid, as observed from a steep pH gradient during chamber formation (De Nooijer et al., 2009a; 2014; Toyofuku et al., 2017), implying a barrier between the site of calcification and the surrounding seawater. This mechanism was recently confirmed by FIB-SEM imaging of the site of calcification (Nagai et al., 2018a) confirming the function of earlier reports on an elaborate membrane network delimiting the site of calcification (Angell, 1979; Bé et al., 1979). Active removal and/or blocking of inhibitors of calcite precipitation such as Mg^{2+} and SO_4^{2-} may also be part of the foraminiferal strategy to promote calcite precipitation (Zeebe and Sanyal, 2002). Both of these processes have a major impact on the calcite precipitation rate and element incorporation. Recently, meta-stable pre-cursor phases were observed in foraminifera during calcification, suggesting crystal growth rates should be faster than classical monomer-addition (Jacob et al., 2017). High rates through a pathway involving an amorphous pre-cursor phase would greatly affect element incorporation (Littlewood et al., 2017). Constraining the rate of calcium carbonate precipitation is hence pivotal for understanding element partitioning in foraminiferal shell carbonate.

Here we determine calcification rates during the formation of single foraminiferal chamber walls by measuring the added shell wall thickness over time. We used pH probing to monitor the duration of the chamber formation event and combined it with the addition and removal of Sr-label at set time-intervals to quantify the thickness of the calcite layer formed during each event (Fig. 1). Visualization of the Sr-label by Nanoscale Secondary Ion Mass Spectrometry (NanoSIMS) of cross-sections of the newly formed chamber subsequently allowed calculating precipitation rates during chamber formation and comparison to the within-wall element signal (Fig. 2). We determined the rates in the low-Mg calcite of the benthic foraminifer *Ammonia beccarii*, which is used as a model-species for many studies on foraminiferal biomineralization, foremost due to its relatively high resilience to varying environmental conditions (De Nooijer et al., 2009b; Nehrke et al., 2013; Toyofuku et al., 2017). Moreover, its elemental composition, and specifically its low Mg content, closely resembles that of planktic species popular in climate reconstructions. We compare our results to inorganic calcite precipitation studies and put in perspective to what extent precipitation rates and element incorporation in this species are biologically controlled.
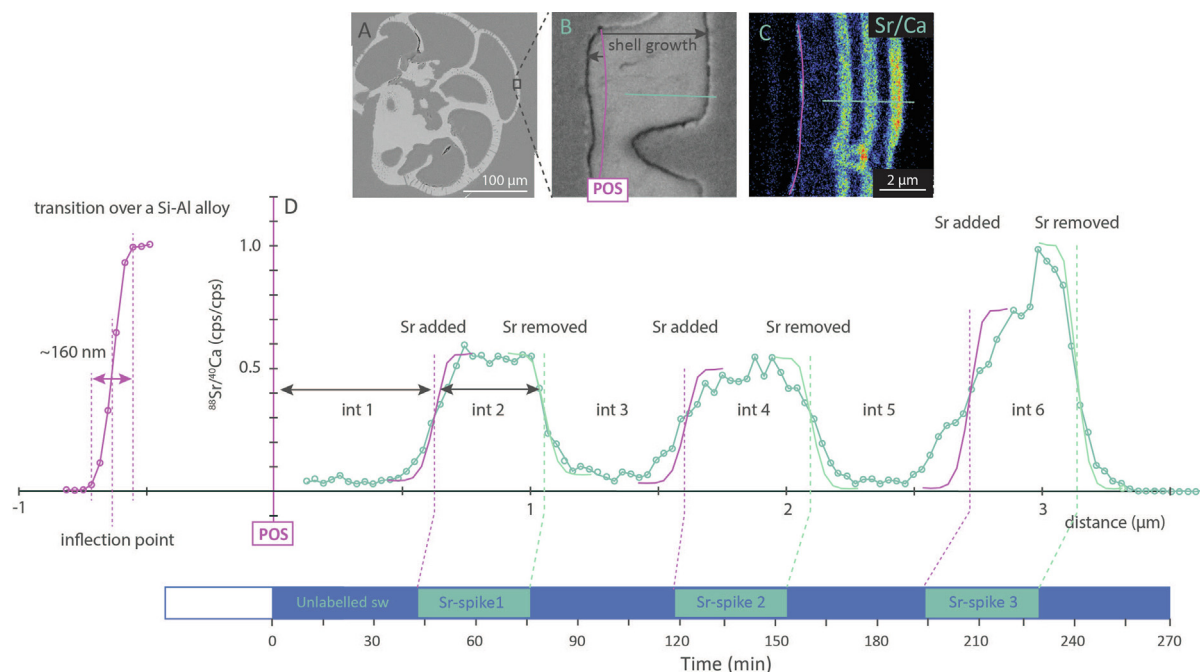
Fig. 1. Quantification of the calcification rate in foraminifera through imaging of the calcite shell following an incubation of live specimens in a medium spiked with Sr label. The calcite chambers (**Panel A**) were exposed by resin-embedding and polishing. Close up of the newly formed chamber (**Panel B**) revealed the position of the primary organic sheet (POS) and the thin inward and more extensive outward precipitated calcite layers. Sr/Ca image (**Panel C**) and lateral profile (**Panel D**) of the newly formed chamber revealed correspondence between Sr incorporated into the calcite shell and the Sr-label spikes in the incubation medium. The magenta line illustrates the spatial resolution of the probing primary ion beam (~160 nm), as determined from the nanoSIMS measurement across a sharp-edged Si particle embedded in an Al alloy using the same machine settings as those used for the foraminifera shell measurements. The calcification rate (μm/h) was calculated by dividing the distance between the consecutive inflection points in the Sr/Ca profile and the duration of the corresponding Sr spike in the medium. Note that the Sr/Ca ratio clearly reached a stable plateau within the Sr-rich and Sr-poor bands. Considering that the duration of the Sr spikes, where the Sr concentration in the incubation medium was constant (high or low), was about 30 min, this shows that a full equilibrium between Sr concentrations in the incubation medium and the SOC was reached within minutes.

2. MATERIALS AND METHODS

2.1. Sample collection and culturing

Living foraminifera were collected from brackish-water salt marsh sediments of Hiragata Bay, Natsushima-cho Yokosuka, Japan (35° 19′21″N, 139° 38′5″E), in spring of 2015. Surface (top ~5 mm) sediments were collected by hand into a plastic bucket and transported to the laboratory to serve as a stock from which individuals of the shallow benthic calcareous foraminifera *Ammonia beccarii* (sensu De Nooijer et al., 2009b) were isolated. This study was conducted using a breeding stock (Lab stock name: Am-S) asexually reproduced from a single individual. Specimens of *Ammonia beccarii* were isolated and fed with fresh algae *Dunaliella salina*. After offspring, a large number of individuals (~300) were distributed over ~30 Petri dishes and were cultured until reaching the size of ~10 chambers. Every evening, debris in the Petri dishes was removed, the 0.2 μm filtered natural seawater was replaced, and fresh *D. salina* was supplied.

2.2. Incubation experiments with variable seawater Sr concentrations

Every morning, specimens were monitored for signs of upcoming chamber formation events, which can be recognized by pseudopodia being subtracted and by the placement of protective cyst (consisting of algae-debris) in a circle around the chamber-to-be-formed and eventually the extrusion of cytoplasm and formation of the primary organic sheet (POS; Angell, 1979; Bé et al., 1979; Nagai et al., 2018a). When there were early signs of an upcoming chamber formation event, the pH-microelectrode and reference electrode were set-up in the vicinity of the new chamber. During chamber formation, commonly lasting between 4 and 7 hours, images were taken with cross-polarized light microscopy to monitor the onset of calcite precipitation and ongoing chamber thickening. After the POS was formed, a decrease in pH (~0.2) indicated the start of chamber formation, which was confirmed by the appearance of a thin birefringent layer at the POS around 10 minutes later (Appendix A). The pH in the foraminiferal
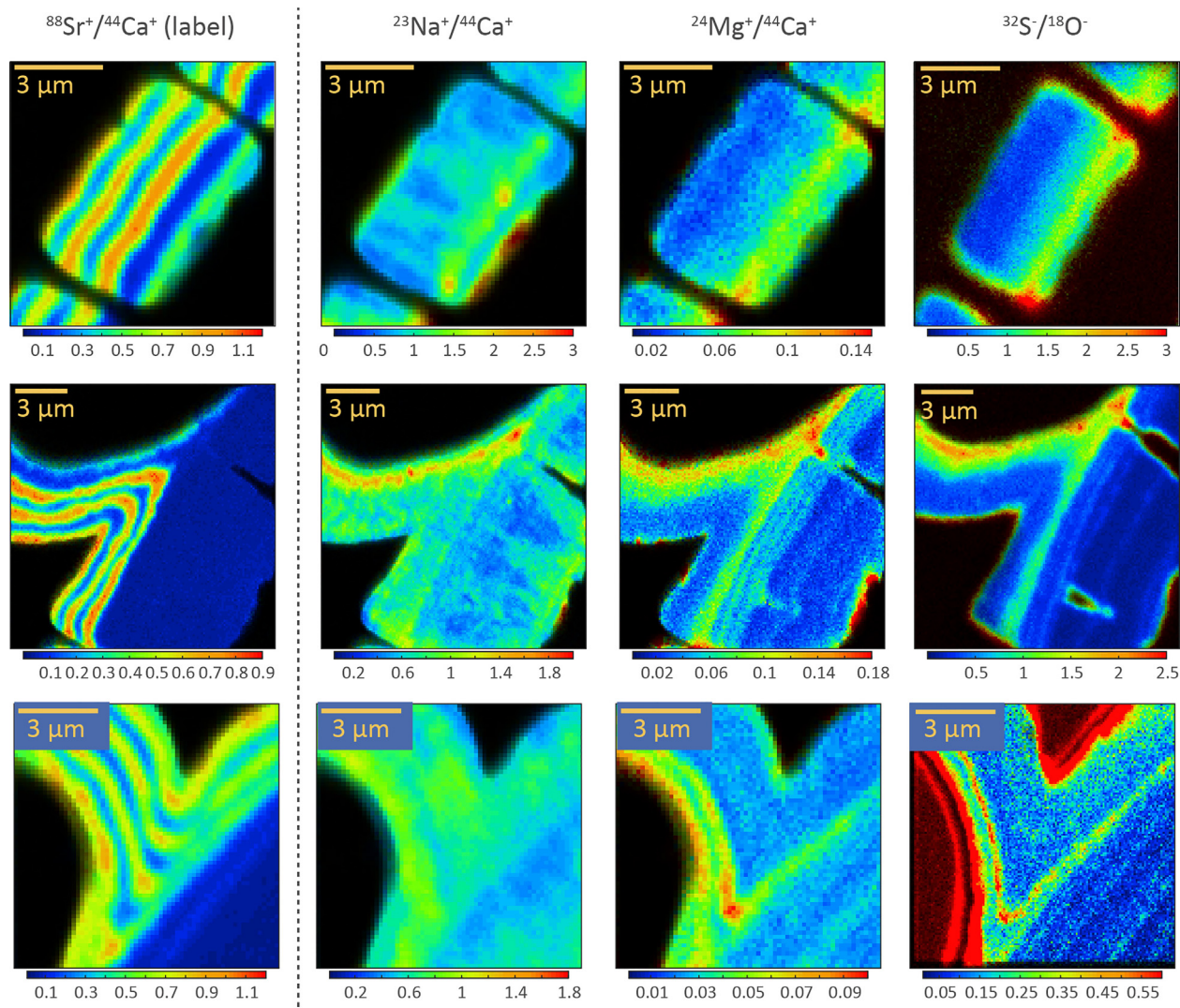
Fig. 2. NanoSIMS images showing the Sr labelling (left) and the natural variability in Na/Ca, Mg/Ca (middle panels) and S/O (right) within walls of three specimens of *Ammonia beccarii*. Note that the measurements shown here were obtained with about a 4-fold larger probing beam (spatial resolution of ∼600 nm) due to a different source of O⁻ primary ions used.

micro-environment was measured near the outer membrane of the site of calcification (maximum of ∼10 µm away, Appendix A), to determine the exact start of calcite formation and to monitor the relationship between pH and calcification rate. This was done with a calibrated pH-microsensor (Unisense A/S Denmark; tip-diameter of 10–25 µm), a reference electrode and a robotic arm as previously described (Glas et al., 2012).

For the incubations, a Sr-enriched stock solution was made by adding 2.215 mg of $SrCl_2$ salt (197-04205, FUJI-FILM Wako pure chemical corporation) to 200 g of distilled water (milli-Q). At set intervals, two consecutive 'spikes' of 150 µL of the Sr-enriched stock solution were added to the Petri dish, containing 15 ml of 0.2 µm filtered natural seawater (Fig. 1; Appendix A). The spikes increased the Sr concentration 20 times, resulting in detectable shell concentrations, without seemingly hampering foraminiferal

growth since the spiked and non-spiked periods were of similar timing and resulted in a similar banding width (see Results). Between spikes, the media in the Petri dishes were replaced with 'un-spiked' 0.2 µm filtered natural seawater. This spiking procedure was repeated until chamber formation was completed, as indicated by the specimen extruding its pseudopodia and starting to move again.

2.3. Sample preparation

After the incubation, each specimen was removed from the Petri dish and shortly placed into double de-ionized water for gentle rinsing to terminate calcification. Subsequently, the specimen was treated with a buffered 1% H_2O_2 solution and heated to 90 °C to remove cytoplasm. Finally, it was embedded in epoxy resin (Araldite 2020), cured for 24 hours at 60 °C and polished. Polishing was

done using silicon carbide wet grinding papers with decreasing coarseness (HERMES, WS Flex 18C, 230 mm, P 800 and 219 ATM, SIC wet grinding paper, grain 4000). This resulted in a cross-sectioned sample with the newly formed chamber wall exposed perpendicular to the shell walls, as evaluated by light microscopy. Careful polishing kept the exposed cross-section within 10% of the plane that crosses the center of the new chamber (Appendix B), because slightly deeper or shallower sections would have resulted in planes that are exposed with a skew. With a maximum of 10% offset in depth, the increase in the wall thickness, and hence in the estimated precipitation rate, was below $\sim$2%. Exposed cross sections were subsequently fine-polished using agglomerated alpha alumina powder (Struers AP-A powder, grain size 0.3 μm) and SiO_2 powder (Logitech SF1 Polishing Suspension, grain size 0.035 μm). Finally, the polished samples were ultrasonically cleaned with ethanol and coated with a 20 nm gold layer using a sputter coater (JEOL JFC-2300HR high resolution fine coater and JEOL FC-TM20 thickness controller).

2.4. Analysis by SEM and NanoSIMS

Imaging analyses by scanning electron microscopy (SEM) and nanometer-scale secondary ion mass spectrometry (nanoSIMS) were performed at Utrecht University. SEM imaging was done with a Jeol Neoscope II JCM-6000 instrument (Jeol, Japan) using a backscattered electron detector. SEM images were taken to identify areas suitable for NanoSIMS imaging and to locate the POS and subsequent organic linings. NanoSIMS analysis was performed with the Cameca NanoSIMS 50L instrument (Cameca, France). Using an element standard (SPI Supplies, 02757-AB 59 Metals & Minerals Standard), magnetic field and exact positions of the electron multiplier detectors were adjusted to enable detection of either positive ($^{23}Na^+$, $^{24}Mg^+$, $^{42}Ca^+$, $^{44}Ca^+$, $^{88}Sr^+$) or negative ($^{16}O^-$, $^{32}S^-$) secondary ions. The positively and negatively charged secondary ions were detected using an 8 keV primary O^- and Cs^+ ion source, respectively. First, areas of interest were pre-sputtered until secondary ion counts stabilized. The same pre-sputtering protocol was used on all samples to ensure comparability among different fields of view (FOV) measured. Subsequently, ion count images were acquired by rastering the primary beam over the sample surface (areas between 8 × 8 and 40 × 40 μm in size) using the following diaphragm and slit settings: D0-2, D1-3, ES-2, AS-0 and EnS-0 for the O^- beam, and D0-0, D1-3, ES-2, AS-2 and EnS-1 for the Cs^+ beam. These settings yielded a primary beam current at the sample surface of $\sim$2 pA (O^-) and $\sim$1 pA (Cs^+) and the corresponding spatial resolution of $\sim$600 nm (O^-) and $\sim$100 nm (Cs^+). Additionally, these settings allowed high transmission while maintaining a sufficient mass resolution to separate isobaric interferences with the exception of the $^{44}Ca_2^+$ (^{44}Ca dimer) on mass 88. The contribution of ^{44}Ca to ^{88}Sr is expected to be less than 1% (estimated from the $^{44}Ca^+$ ion counts following assumptions as in Gabitov et al. (2013), modified for isotopic abundance) and was not corrected for since the ^{88}Sr ion counts are not used for quantitative purposes. Secondary ions were

detected with a dwell time of 2 ms/pixel (positive ions) and 0.8 ms/pixel (negative ions). To increase the overall signal, the same FOV was imaged multiple times (200–1000), and the resulting ion count images were aligned and accumulated.

While the spatial resolution of the primary O^- beam afforded by the above instrument settings was sufficient to resolve the Sr peaks within the chamber wall and link their separation to the separation of the Sr spikes during the incubation experiment, it was insufficient to resolve whether an equilibrium between the seawater and the SOC was reached *within* the interval when the seawater Sr concentrations were constant (high or low). Therefore, additional nanoSIMS images were acquired with the new-generation O^- Hyperion RF-plasma source. Using the diaphragm and slit settings of D0-4, D1-5, ES-3 and AS-2, the spatial resolution of the O^- primary beam (current of 0.1 pA) was decreased down to $\sim$160 nm, as determined from the measurement of a certified standard (Si particles embedded in an Al alloy; MBH-54X GS20J1, ARMI/MBH Analytical Ltd.) recommended by Cameca to quantify the lateral resolution of the probing beam. The standard was cut to fit the nanoSIMS holder and polished to $\sim$0.035 μm roughness.

2.5. Data processing

NanoSIMS data were processed using the freeware program Look@NanoSIMS (Polerecky et al., 2012) as well as additional custom-made routines in Matlab. Element maps are presented as El/Ca and El/O ion count ratios for the positively and negatively charged secondary ions, respectively. With the exception of organic linings, the Ca/O ratio is fixed in the shell wall, and since the detected O^- secondary ions are homogeneous throughout the calcite shell, the El/O ratios are a good proxy for the El/Ca ratios for the elements that can only be measured with the Cs^+ beam.

2.6. Calculation of calcification rates

Calcification rates were determined from lateral profiles extracted from the images of the Sr label. The profiles were taken along lines oriented perpendicularly to the Sr-enriched bands avoiding pixels close to edges, cracks, or pores within the shell wall. The width of the lateral profiles was set to 10 pixels to improve signal-to-noise ratio. First, inflection points were determined by fitting the Sr-label profiles with a spline and calculating where the second derivative of the spline equals zero. Subsequently, the calcification rate was determined by dividing the distance between the consecutive inflection points and the duration of the corresponding time interval where the Sr-label was added to or removed from the incubation medium (Fig. 1; Appendix A). Finally, foraminiferal calcification rates were converted into fluxes using the calcite specific density of 2.71 g/cm^3 and molar weight of 100 g/mol (Appendix B). This approach assumes laminar addition of calcite in the direction perpendicular to the POS, which is confirmed by the fairly straight and parallel Sr bands observed in the nanoSIMS images (Fig. 2). It is important to note here that pre-

cipitation rates estimated by this approach could be slightly different; if the growing crystal front has a higher surface area, estimated rates would decrease. Additionally, this approach is independent of the spatial resolution with which the Sr profiles are determined as long as it is sufficient to resolve the multiple neighboring Sr bands within the shell wall.

3. RESULTS

3.1. Calculating foraminiferal precipitation rates

All NanoSIMS images of the cross-sectioned newly formed chambers consistently show Sr-labelled bands parallel to the inner and outer surface of the shell wall (Figs. 1 and 2; Appendix A). Within the shell wall, ~3–4 Sr-enriched layers are visible, placed at regular intervals, reflecting the timing of the Sr-spikes (i.e., label) in the culture medium (Fig. 1). The 'banded' pattern is in accordance with laminar calcite addition in this group of foraminifera onto the 'primary organic sheet' (POS), an organic template that is secreted prior to calcification (Banner et al., 1973; Spero, 1988; Geerken et al., 2019). Calcification first occurs bi-directionally, with the first Sr-label being deposited at both the inside and outside of the POS (Appendix A and Fig. 2). Consecutive Sr-enriched layers are observed exclusively on the outer calcite layer, showing that the subsequent calcification occurs uni-directionally (i.e. towards the outer surface of the chamber wall) with on-going chamber formation.

Based on the assumption of a laminar calcite addition, shell-wall growth of the newly formed chambers over time is similar among specimens, at ~0.538 ± 0.073 µm/h (mean +/- 1 SD of average rates per specimen), using Sr-profiles of 13 NanoSIMS images from 5 specimens (Fig. 3). Conversion of these values into fluxes yielded precipitation rates of ~24 ± 5 nmol/cm^2/min (Appendix C). During the precipitation of a new chamber, the previously built chambers are also covered with a new layer of calcite (Erez, 2003; Nehrke et al., 2013). New calcite lamella for some individuals extend over the entire specimen, but in others only over the neighbouring chambers (Nehrke et al., 2013). Our data show that the Sr-enriched bands within this additional layer become thinner (Fig. 4), suggesting slower precipitation rates away from the newly added chamber. However, this decrease in rates could not be well constrained due to an insufficient spatial resolution of our measurements.

Previously reported rates (0.6–80 nmol/cm^2/min for planktonic and ~1.33–430 nmol/cm^2/min for benthic species) were based on alkalinity measurements and assumed continuous calcification (Erez, 1983; Anderson and Faber, 1984). Duration of chamber addition events has been previously determined for *A. beccarii* using pH-microelectrodes, recording a pH drop during chamber addition (Glas et al., 2012), comparable to the decrease in pH reported here (Appendix A). However, this approach assumed a constant thickness of 3 µm for the new chamber. Converting the rates reported in (Glas et al., 2012) using a shell thickness of 3 µm and the range of observed calcification times, yields an average rate of ~33 nmol/h. Due to differences in measured duration of calcification versus a constant assumed increase in shell thickness, these rates may vary between 19 and 135 nmol/h. Our approach incorporates both chamber thickness and time control during a chamber formation
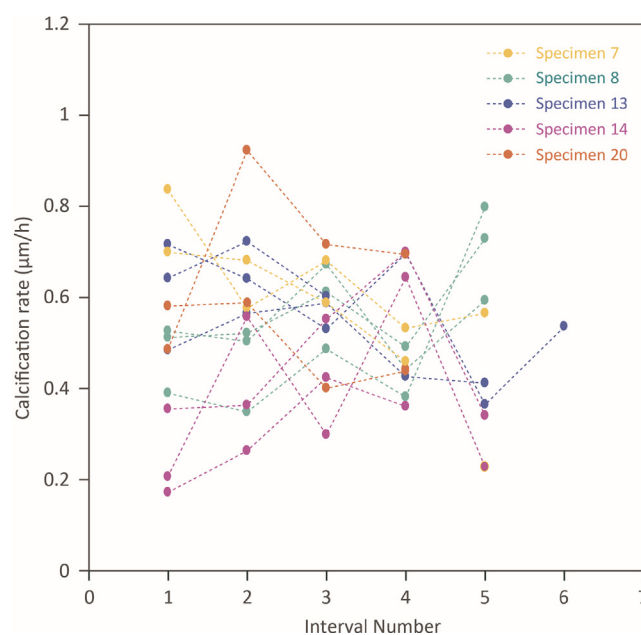

Fig. 3. Calculated calcification rates (µm/h) for time-intervals within the shell walls of *A. beccarii*, where interval '1' is the interval next to the POS and only the layer precipitated towards the outside is considered. Number of images = 13, number of specimens = 4. The rate of interval 1 is significantly lower than later intervals (for percentage change between intervals, averaged per specimen p-value = 0, F-test = 5.9 * 10^16, MATLAB 'multcompare' test based on ANOVA).
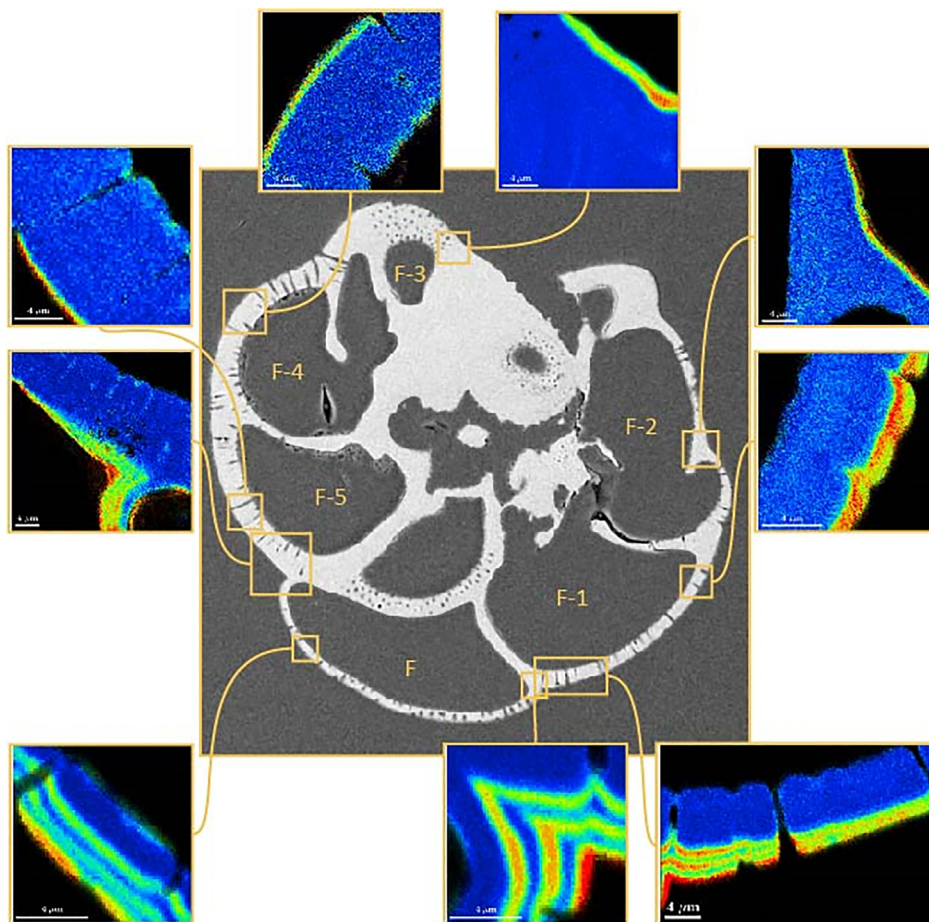
Fig. 4. Compilation showing SEM image of the polished cross-section of an *A. beccarii* specimen embedded in resin, location of NanoSIMS images indicated with yellow squares) and NanoSIMS Sr-images of the penultimate chamber (F), ultimate chamber (F-1) and at various chambers and their intersections across the rest of the shell (F-2 to F-6). The Sr-labels are observed in the penultimate chamber, however the spacing of the bands is approximately halved compared to that in the ultimate (F) chamber.

event. Hence, the rates determined here are more accurate and precise compared to previous estimates. Furthermore, our results are the first indication that precipitation rates are similar among specimens.

At a scale smaller than the spatial resolution of our technique, the POS may be slightly undulating (Spero, 1988; Nagai et al., 2018b), which may somewhat increase the surface area upon which the first calcite nucleates. However, the potential effect of an undulating organic matrix and concomitant undulating calcite growth front on the estimated precipitation rate is likely minor, as eventually the integrated net growth is unidirectional, from the POS towards the outside, resulting in a smooth shell surface. The incorporation of time-controlled Sr-spikes in this study confirms that the chamber growth front runs parallel to the POS (Fig. 2). Unidirectional growth is furthermore confirmed by focused ion-beam observations of the site of calcification (SOC) of specimens captured during different stages of chamber formation, which shows that calcite is deposited on the POS at the onset of chamber formation and extends towards the outer membrane in later stages of calcification (Nagai et al., 2018a).

4. DISCUSSION

4.1. Foraminiferal and inorganic calcite precipitation rates

The foraminiferal precipitation rates observed here are relatively high compared to those reported for many inorganic precipitation experiments. The inorganic precipitation rates depend on solution chemistry, whereby higher rates are obtained (1) in the absence of calcification inhibitors such as Mg^{2+} and SO_4^{2-}; (2) at high $CaCO_3$ saturation states (Fig. 5); and (3) at a seawater $[Ca^{2+}]:[CO_3^{2-}]$ stoichiometry close to one (Nehrke et al., 2007). The relatively high precipitation rates by foraminifera may hence be obtained by a combination of these factors. Most inorganic calcite precipitation experiments using seawater-like solutions show lower rates (0.06–8.5 nmol/cm²/min; Erez, 1983; Anderson and Faber, 1984) than those observed here for foraminifera. Foraminiferal precipitation rates are more in line with inorganic calcite precipitation studies using Mg-free solutions, with rates ranging from 0.16 to 90 nmol/cm²/min (Tesoriero and Pankow, 1996; Nehrke et al., 2007; Tang et al., 2008; Fig. 5). This is consistent with the strong
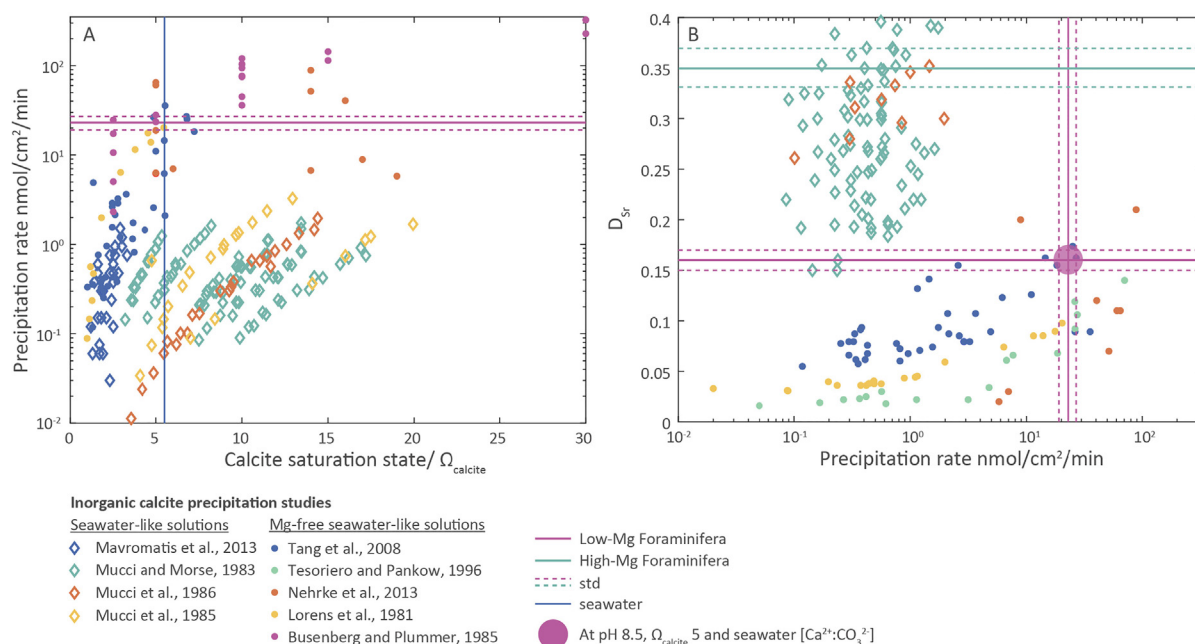
Fig. 5. **Panel A.** Precipitation rates for inorganic precipitation studies, with open diamonds showing results for experiments with seawater-like solutions containing Mg and closed circles representing Mg-free seawater-like solutions, against solution omega, with seawater omega indicated by a red dashed line for comparison. **Panel B.** Sr partitioning (D_{Sr}) of inorganic precipitation studies against precipitation rate, with open diamonds showing results from experiments using seawater-like solutions containing Mg and closed circles Mg-free seawater-like solutions. Foraminiferal D_{Sr} (Van Dijk et al., 2017b) and precipitation rates obtained in this study are indicated with blue lines for low Mg species. Foraminiferal D_{Sr} for high Mg species (Van Dijk et al., 2017b) are indicated with green lines, precipitation rates are unknown. The larger spot on the right side indicates what precipitation rate fits the observed D_{Sr} for low- and high-Mg/Ca foraminifera, where it is assumed that the fluid from which the calcite precipitates has a pH of 8.5, an omega of 5 and a $Ca^{2+}:CO_3^{2-}$ of open ocean surface seawater.

fractionation against Mg in most foraminifera, including the species studied here.

The relationship between the precipitation rate and Sr incorporation from inorganic experiments can be used to explain foraminiferal precipitation rates (Lorens, 1981; Böhm et al., 2012). The estimated precipitation rates for Sr/Ca ratios found in *A. beccarii* (and in most other low-Mg/Ca foraminifera) provides a minimum value of 17 and a best estimate at 26 nmol/cm^2/min, which fit our observation of 24 nmol/cm^2/min remarkably well. Moreover, this agreement implies that the distribution coefficient for Sr (D_{Sr}) is in line with the observed low-Mg contents (Geerken et al., 2018; Fig. 5) and that foraminifera precipitate their calcite at non-equilibrium rates and kinetic effects explain the relatively high Sr incorporation (Böhm et al., 2012). Moreover, the strong dependency of Na/Ca in inorganic precipitated calcite on precipitation rate compared to the $(Na^+)^2/Ca^{2+}$ activity ratio (Devriendt et al., 2021), suggest the same precipitation rate for *Ammonia sp.* as that found here.

The slope between the precipitation rate and D_{Sr} is also influenced by pH, whereby a higher pH increases D_{Sr} (Tang et al., 2012). The best fit between foraminiferal as well as inorganic D_{Sr} with the precipitation rate is obtained for a relatively high pH of ~8.5 (Tang et al., 2012). This agrees with observations of an elevated intra-cellular pH (~8.5–9) in foraminifera (Bentov et al., 2009; De Nooijer et al.,

2009a). Our results also suggest that the Sr/Ca at the SOC is similar to that of the surrounding seawater, which is confirmed by Ca and Sr isotope fractionation (Böhm et al., 2012). This conclusion is also supported by our NanoSIMS results obtained with the highest spatial resolution (~160 nm), showing a near-instantaneous uptake of Sr from the seawater into the calcifying fluid (Fig. 1).

Other factors that have been suggested to control foraminiferal element incorporation are $CaCO_3$ phase transformations (Jacob et al., 2017), involvement of organic templates and molecules (Branson et al., 2016), and biological control on the element chemistry of the site of calcification (Elderfield et al., 1996; Erez, 2003; Nehrke et al., 2013; De Nooijer et al., 2014; Toyofuku et al., 2017). To maintain a seawater-like saturation state in the SOC, which is kept secluded from seawater by a network of membranes (Nagai et al., 2018a), Ca^{2+} and CO_3^{2-} need to be continuously supplied to the SOC. As Ca^{2+} is taken up directly during calcification in *Ammonia* (Nehrke et al., 2013), Ca^{2+} pumps or channels may well be involved in this species' biomineralization (Toyofuku et al., 2017), similar to those responsible for calcification in scleractinian corals (Gagnon et al., 2007). Involvement of Ca-pumps explains our observation of Sr reaching the SOC directly, since Ca^{2+} pumps are suggested to be permeable for Sr^{2+} (Gagnon et al., 2007). Since such pumps are unlikely equally permeable to all cations, spiking with other ions would result in a less pronounced banding.

Ca-pumping is also consistent with a recently proposed model for foraminiferal calcification (Toyofuku et al., 2017), which proposes that during calcification, calcium ions (pumped in) are exchanged for protons (going out), resulting in a strong pH gradient that drives inward CO_2 diffusion. If this DIC supply to the SOC matches the inflow of calcium, as suggested by a relatively constant proton flux over time (Toyofuku et al., 2017), the saturation state in the SOC remains relatively high and the Ca:DIC stoichiometry close to 1. Both these factors promote the relatively high and constant foraminiferal precipitation rate as observed here. The possible involvement of seawater as a source of the ions for biomineralization is discussed in the final section of the Discussion.

For elements that are excluded from the SOC during calcification, such as Mg^{2+}, foraminiferal element partitioning cannot be directly compared to that from abiotic studies, because El/Ca (Element/Ca^{2+}) ratios in the SOC are altered compared to seawater. Limited transport of some elements by transmembrane Ca^{2+}-pumps could be due to differences in charge (e.g., for Na^+) and ionic radius (e.g., for (hydrated) Mg^{2+}). The resulting element composition of the SOC will likely influence precipitation rates and hence incorporation of these elements.

4.2. Intra-shell variability

Our results show that calcification rates do not change during the chamber formation event (Fig. 3 and Appendix C). Hence, it is unlikely that element banding within chamber walls, as reported for many elements and many species (e.g. Kunioka et al., 2006; Spero et al., 2015; Geerken et al., 2019), reflect differences in precipitation rate, at least within the resolution of our Sr-spikes intervals. We cannot fully exclude a variability in rate within the first ∼0.5 μm of the newly precipitated calcite layer and a its potential correlation to high El/Ca near the POS. Since elevated El/Ca (e.g. Mg/Ca, Na/Ca, K/Ca) bands are ∼1 μm wide in *Ammonia* spp. (this study, Fig. 2; Geerken et al., 2019), there is unlikely a relation between these bands and variable precipitation rates. Location of the POS in the first band may also affect the estimated rates (Bonnin et al., 2019), but likely only plays a minor role due to the constant Ca/O ratio throughout the shell wall.

Whereas precipitation rate does not explain the elevated El/Ca during the early stage of foraminiferal chamber wall formation, initial presence of seawater-like ion concentrations at the SOC may explain enhanced trace element incorporation in the first carbonate precipitated. Such initially elevated El/Ca ratios at the SOC would result in so-called 'element banding' around the POS (Fig. 2; Geerken et al., 2018; 2019). Element banding towards the end of chamber wall formation might in turn be explained by a combination of Rayleigh fractionation and a decrease in Ca^{2+} fluxes towards the end of chamber formation (Elderfield et al., 1996). Involvement of seawater furthermore explains why element banding is not limited to specific elements, but observed for a wide array of elements (Kunioka et al., 2006; Van Dijk et al., 2017a; Geerken et al., 2018; 2019). Such a mechanism suggests an element banding particularly strong

for elements with a low partition coefficient, related to a strong biological control that limits their transport into the SOC, such as Mg^{2+}, while Ca^{2+} is transported inwards (Geerken et al., 2019). The concentration of calcite growth inhibitors in the SOC thus appears to be actively reduced to enhance calcification (Fig. 2; Zeebe and Sanyal, 2002; Erez, 2003). The mechanism by which foraminifera control ion concentrations in the SOC may differ among species but is crucial in explaining the element composition of their calcite and their dependency on environmental parameters. Further studies may therefore test which other elements, besides Sr and Ca, reach the SOC directly during calcification and whether the inward transport of ions differs among species.

4.3. Implications for foraminiferal biomineralization and proxies

Our findings, combined with previously published results, suggest a model of low-Mg/Ca, benthic foraminiferal calcification that is characterized by two major processes (Fig. 6). During calcification, ions are transported from the surrounding seawater into the SOC. The exact (selective) ion transport proteins include a V-type ATPase that exchanges Ca^{2+} for (two) H^+ and likely induces an inward diffusion of CO_2 as the main carbon source (Toyofuku et al., 2017). The accompanying elevated internal pH promotes calcite precipitation rates and helps explain the rates reported here. It could be that Sr^{2+} is transported like Ca ions by this transporter and hence the Sr/Ca outside the foraminifer is translated directly to the Sr/Ca in the SOC. The sharp increase and decrease of the Sr/Ca in the foraminiferal shell, as observed during our 'spiking' experiment, suggest that the residence time of Sr^{2+} in the SOC is very short. Based on the spatial resolution of our images, the time lag between Sr spiking and Sr incorporation appears to be not more than 10 minutes (Fig. 1), suggesting a residence time of Sr^{2+} in the SOC of at most about five minutes. In any case, the difference in elemental composition between inside and outside, as well as the isotopic difference between seawater and SOC of these elements, is determined by ion channels or pumps and thus biologically controlled. Subsequently, precipitation of $CaCO_3$ and element partitioning from the SOC may well be largely determined by thermodynamics and process kinetics (Fig. 6), for which the rate of calcite precipitation is one of the important parameters (Fig. 5). Thermodynamic control will furthermore cause additional partitioning and fractionation of the incorporated Sr^{2+}, Mg^{2+}, $B(OH)_4^-$, and other ions. Environmental effects on element incorporation or isotope fractionation therefore can influence either the biological component (i.e., the active transport of ions) or the kinetics of the $CaCO_3$ precipitation, or both. Salinity, for example, may well affect the amount of Na^+ transported into the SOC due to a higher Na^+ concentration directly outside the foraminifer, but this increase unlikely affects the precipitation dynamics. Temperature, however, may affect the transport of Mg^{2+} into the SOC, but has in any case a positive effect on its incorporation from the SOC's fluid into the $CaCO_3$ (Branson et al., 2013). Specific organic compounds have been proposed to
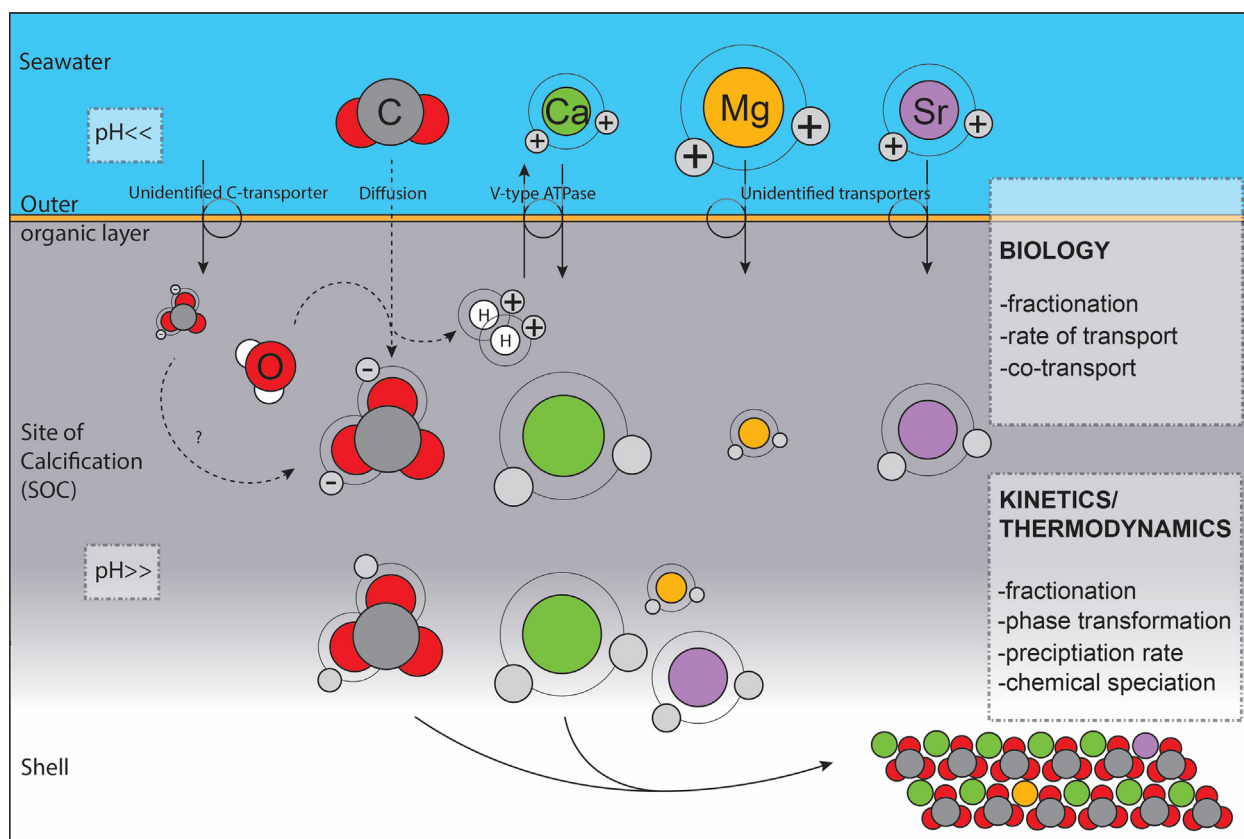
Fig. 6. A 'cascade model' of element incorporation during low-Mg/Ca Rotaliid foraminiferal biomineralization. Ions are transported over the so-called outer organic layer from the surrounding seawater into the SOC. This alters the ratio between the ions since this step likely involves selective ion transporters, resulting in e.g. a relatively low $[Mg^{2+}]$ in the SOC. Secondly, the concentration (and ratio) of the ions in the SOC determine kinetics and thermodynamic processes that result in the precipitation of $CaCO_3$. The DIC is supplied by diffusion over the protective envelope due to the strong pH gradient as a result of the Ca^{2+}/H^+ exchange. This simplified model does not consider the proposed involvement of seawater as a source of ions, either in intermediate- and high-Mg/Ca Rotaliid foraminifera, or the involvement of seawater contributing ions at the start of chamber formation (see text for a more elaborate explanation). For clarity, the model presented here also omits the potential impact of specialized organic templates, and the possibility of other inorganic carbon transport routes.

help calcite nucleation (Towe and Cifelli, 1967; Wetmore, 1999), which may further affect the precipitation dynamics and the initial precipitation rate.

Not all foraminiferal species precipitate calcite with a low-Mg content like *A. beccarii* studied here. Species precipitating calcite with a higher Mg content may hence have a SOC more open to seawater which raises Mg concentrations, in line with observations of seawater vacuolization in intermediate-Mg foraminiferal species (Bentov et al., 2009). This may also explain why higher-Mg species also show higher concentrations of most other ions, such as Na^+, SO_4^{2-}, and Sr^{2+} (Van Dijk et al., 2017b) and more apparent element banding (Geerken et al., 2019). The positive correlation between Sr and Mg among foraminiferal species has also been explained by a lattice effect related to Mg-uptake, whereby Mg ions distort the calcite lattice allowing more Sr to be incorporated (Mucci and Morse, 1983), as is observed in abiotic calcite precipitation studies (Fig. 5). Foraminifera with a relatively high Mg^{2+} content may hence precipitate at lower rates due to the inhibitory effect of Mg^{2+}, while incorporating more Sr^{2+} due to the lower lattice strain effect. This may hence resolve the appar-

ent contradiction of higher D_{Sr} found in specimens with lower precipitation rates (Erez, 2003). When the impact of precipitation rate would be fully resolved for elements present in the SOC, the El/Ca ratio during calcification can be inferred. Our study hence highlights the need for quantification of inorganic element distribution coefficients in experiments at high non-equilibrium rates, possibly including transient pre-cursor phases and mimicking conditions in the SOC as much as possible.

5. CONCLUSIONS

(1) Precipitation rates during chamber formation in the benthic foraminifer *Ammonia beccarii* were determined using a spiking experiment with Sr^{2+} and subsequent visualization of the incorporated label using NanoSIMS. The results were used to assess the impact of precipitation rates on element incorporation during calcification in foraminifera. Experimental results and comparison with previously published data lead to the following conclusions:*Ammonia*

beccarii precipitates its calcite at a precipitation rate of 24 ± 4 nmol/cm^2/min. These rates did not change within the chamber wall analysed and hence unlikely explain the element banding within the walls of these foraminifera.

(2) The rates obtained are consistent with the Sr/Ca, given the relatively high internal pH during calcification in this species.

(3) Together with previously published results, calcite precipitation in this foraminifer likely reflects two steps: one that partitions elements (and fractionates isotopes) between seawater and the site of calcification and another that is a function of the physico-chemical conditions at which the foraminiferal calcium carbonate precipitates.

6. RESEARCH DATA

All the raw data on which the results presented here can be found at: https://doi.org/10.4121/13516592.

Declaration of Competing Interest

The authors declare that they have no known competing financial interests or personal relationships that could have appeared to influence the work reported in this paper.

APPENDIX A. SUPPLEMENTARY MATERIAL

Supplementary data to this article can be found online at https://doi.org/10.1016/j.gca.2021.11.026.

REFERENCES

Anand P., Elderfield H. and Conte M. H. (2003) Calibration of Mg/Ca thermometry in planktonic foraminifera from a sediment trap time series. *Paleoceanography* 18.

Anderson O. R. and Faber W. W. (1984) An estimation of calcium carbonate deposition rate in a planktonic foraminifer *Globigerinoides sacculifer* using ^{45}Ca as a tracer; a recommended procedure for improved accuracy. *J. Foraminifer. Res.* 14, 303–308.

Angell R. W. (1979) Calcification during chamber development in *Rosalina floridana. J. Foraminifer. Res.* 9, 341–353.

Banner F., Sheehan R. and Williams E. (1973) The organic skeletons of rotaline foraminifera; a review. *J. Foraminifer. Res.* 3, 30–42.

Bé A. W., Hemleben C., Anderson O. R. and Spindler M. (1979) Chamber formation in planktonic foraminifera. *Micropaleontology* 25, 294–307.

Bentov S., Brownlee C. and Erez J. (2009) The role of seawater endocytosis in the biomineralization process in calcareous foraminifera. *Proc. Natl. Acad. Sci. USA* 106, 21500–21504.

Böhm F., Eisenhauer A., Tang J., Dietzel M., Krabbenhöft A., Kisakürek B. and Horn C. (2012) Strontium isotope fractionation of planktic foraminifera and inorganic calcite. *Geochim. Cosmochim. Acta* 93, 300–314.

Bonnin E. A., Zhu Z., Fehrenbacher J. S., Russell A. D., Hönisch B., Spero H. J. and Gagnon A. C. (2019) Submicron sodium banding in cultured planktic foraminifera Shells. *Geochim. Cosmochim. Acta* 253, 127–141.

Boyle E. A. (1981) Cadmium, zinc, copper, and barium in foraminifera tests. *Earth Planet. Sci. Lett.* 53, 11–35.

Branson O., Redfern S. A. T., Tyliszczak T., Sadekov A., Langer G., Kimoto K. and Elderfield H. (2013) The coordination of Mg in foraminiferal calcite. *Earth Planet. Sci. Lett.* 383, 134–141.

Branson O., Bonnin E. A., Perea D. E., Spero H. J., Zhu Z., Winters M., Hönisch B., Russell A. D., Fehrenbacher J. S. and Gagnon A. C. (2016) Nanometer-scale chemistry of a calcite biomineralization template: Implications for skeletal composition and nucleation. *Proc. Natl. Acad. Sci. USA*, 201522864.

Burton E. A. and Walter L. M. (1991) The effects of PCO_2 and temperature on magnesium incorporation in calcite in seawater and MgCl$_2$-CaCl$_2$ solutions. *Geochim. Cosmochim. Acta* 55, 777–785.

Busenberg E. and Plummer L. N. (1985) Kinetic and thermodynamic factors controlling the distribution of SO_3^{2-} and Na^+ in calcites and selected aragonites. *Geochim. Cosmochim. Acta* 49, 713–725.

Culver S. J. (1991) Early Cambrian foraminifera from west Africa. *Science* 254, 689–691.

De Nooijer L. J., Toyofuku T. and Kitazato H. (2009a) Foraminifera promote calcification by elevating their intracellular pH. *Proc. Natl. Acad. Sci. USA* 106, 15374–15378.

De Nooijer L. J., Langer G., Nehrke G. and Bijma J. (2009b) Physiological controls on seawater uptake and calcification in the benthic foraminifer *Ammonia tepida. Biogeosciences* 6, 2669–2675.

De Nooijer L. J., Spero H. J., Erez J., Bijma J. and Reichart G. J. (2014) Biomineralization in perforate foraminifera. *Earth Sci. Rev.* 135, 48–58.

Devriendt L. S., Mezger E. M., Olsen K. E., Watkins J. M., Kaczmarek K., Nehrke G., De Nooijer L. J. and Reichart G. J. (2021) Sodium incorporation into inorganic CaCO$_3$ and implications for biogenic carbonates. *Geochim. Cosmochim. Acta* 314, 294–312.

Dueñas-Bohórquez A., Raitzsch M., De Nooijer L. J. and Reichart G.-J. (2011) Independent impacts of calcium and carbonate ion concentration on Mg and Sr incorporation in cultured benthic foraminifera. *Mar. Micropaleontol.* 81, 122–130.

Elderfield H., Bertram C. J. and Erez J. (1996) Biomineralization model for the incorporation of trace elements into foraminiferal calcium carbonate. *Earth Planet. Sci. Lett.* 142, 409–423.

Erez J. (1983) *Biomineralization and Biological Metal Accumulation.* Springer, pp. 307–312.

Erez J. (2003) The source of ions for biomineralization in foraminifera and their implications for paleoceanographic proxies. *Biomineralization* **54**, 115–149.

Gabitov R., Gagnon A., Guan Y., Eiler J. and Adkins J. (2013) Accurate Mg/Ca, Sr/Ca, and Ba/Ca ratio measurements in carbonates by SIMS and NanoSIMS and an assessment of heterogeneity in common calcium carbonate standards. *Chem. Geol.* **356**, 94–108.

Gagnon A. C., Adkins J. F., Fernandez D. P. and Robinson L. F. (2007) Sr/Ca and Mg/Ca vital effects correlated with skeletal architecture in a scleractinian deep-sea coral and the role of Rayleigh fractionation. *Earth Planet. Sci. Lett.* **261**, 280–295.

Geerken E., De Nooijer L. J., Van Dijk I. and Reichart G.-J. (2018) Impact of salinity on element incorporation in two benthic foraminiferal species with contrasting magnesium contents. *Biogeosciences* **15**, 2205.

Geerken E., De Nooijer L. J., Roepert A., Polerecky L., King H. E. and Reichart G. J. (2019) Element banding and organic linings within chamber walls of two benthic foraminifera. *Sci. Rep.* **9**, 3598.

Glas M. S., Langer G. and Keul N. (2012) Calcification acidifies the microenvironment of a benthic foraminifer (*Ammonia* sp.). *J. Exp. Mar. Biol. Ecol.* **424**, 53–58.

Jacob D., Wirth R., Agbaje O., Branson O. and Eggins S. (2017) Planktic foraminifera form their shells via metastable carbonate phases. *Nat. Commun.* **8**, 1265.

Knoll A. H. (2003) Biomineralization and evolutionary history. *Rev. Mineral. Geochem.* **54**, 329–356.

Kunioka D., Shirai K., Takahata N., Sano Y., Toyofuku T. and Ujiie Y. (2006) Microdistribution of Mg/Ca, Sr/Ca, and Ba/Ca ratios in *Pulleniatina obliquiloculata* test by using a NanoSIMS: Implication for the vital effect mechanism. *Geochem. Geophys. Geosyst.* **7**.

Littlewood J. L., Shaw S., Peacock C. L., Bots P., Trivedi D. and Burke I. T. (2017) Mechanism of enhanced strontium uptake into calcite via an amorphous calcium carbonate crystallization pathway. *Cryst. Growth Des.* **17**, 1214–1223.

Lorens R. B. (1981) Sr, Cd, Mn and Co distribution coefficients in calcite as a function of calcite precipitation rate. *Geochim. Cosmochim. Acta* **45**, 553–561.

Mavromatis V., Montouillout V., Noireaux J., Gaillardet J. and Schott J. (2015) Characterization of boron incorporation and speciation in calcite and aragonite from co-precipitation experiments under controlled pH, temperature and precipitation rate. *Geochim. Cosmochim. Acta* **150**, 299–313.

Mucci A. and Morse J. W. (1983) The incorporation of Mg^{2+} and Sr^{2+} into calcite overgrowths: influences of growth rate and solution composition. *Geochim. Cosmochim. Acta* **47**, 217–233.

Nagai Y., Uematsu K., Chen C., Wani R., Tyszka J. and Toyofuku T. (2018a) Weaving of biomineralization framework in rotaliid foraminifera: implications for paleoceanographic proxies. *Biogeosciences* **15**, 6773–6789.

Nagai Y., Uematsu K., Wani R. and Toyofuku T. (2018b) Reading the fine print: Ultra-microstructures of foraminiferal calcification revealed using focused ion beam microscopy. *Front. Mar. Sci.* **5**, 67.

Nehrke G., Keul N., Langer G., De Nooijer L. J., Bijma J. and Meibom A. (2013) A new model for biomineralization and trace-element signatures of Foraminifera tests. *Biogeosciences* **10**, 6759–6767.

Nehrke G., Reichart G.-J., Van Cappellen P., Meile C. and Bijma J. (2007) Dependence of calcite growth rate and Sr partitioning on solution stoichiometry: Non-Kossel crystal growth. *Geochim. Cosmochim. Acta* **71**, 2240–2249.

Nürnberg D., Bijma J. and Hemleben C. (1996) Assessing the reliability of magnesium in foraminiferal calcite as a proxy for water mass temperatures. *Geochim. Cosmochim. Acta* **60**, 803–814.

Pawlowski J., Holzmann M., Berney C., Fahrni J., Gooday A. J., Cedhagen T., Habura A. and Bowser S. (2003) The evolution of early Foraminifera. *Proc. Natl. Acad. Sci. USA* **100**, 11494–11498.

Polerecky L., Adam B., Milucka J., Musat N., Vagner T. and Kuypers M. M. M. (2012) Look@NanoSIMS–a tool for the analysis of nanoSIMS data in environmental microbiology. *Environ. Microbiol.* **14**, 1009–1023.

Ridgwell A. and Zeebe R. E. (2005) The role of the global carbonate cycle in the regulation and evolution of the Earth system. *Earth Planet. Sci. Lett.* **234**, 299–315.

Sanyal A., Hemming N. G., Broecker W. S., Lea D. W., Spero H. J. and Hanson G. N. (1996) Oceanic pH control on the boron isotopic composition of foraminifera: evidence from culture experiments. *Paleoceanography* **11**, 513–517.

Schiebel R. (2002) Planktic foraminiferal sedimentation and the marine calcite budget. *Global Biogeochem. Cycles* **16**, 3-1-3-21.

Spero H. J. (1988) Ultrastructural examination of chamber morphogenesis and biomineralization in the planktonic foraminifer *Orbulina universa*. *Mar. Biol.* **99**, 9–20.

Spero H. J., Eggins S. M., Russell A. D., Vetter L., Kilburn M. R. and Hönisch B. (2015) Timing and mechanism for intratest Mg/Ca variability in a living planktic foraminifer. *Earth Planet. Sci. Lett.* **409**, 32–42.

Tang J., Dietzel M., Böhm F., Köhler S. J. and Eisenhauer A. (2008) Sr^{2+}/Ca^{2+} and $^{44}Ca/^{40}Ca$ fractionation during inorganic calcite formation: II. Ca isotopes. *Geochim. Cosmochim. Acta* **72**, 3733–3745.

Tang J., Niedermayr A., Kohler S., Bohm F., Kisakurek B., Eisenhauer A. and Dietzel M. (2012) Sr^{2+}/Ca^{2+} and $^{44}Ca/^{40}Ca$ fractionation during inorganic calcite formation: III. Impact of salinity/ionic strength. *Geochim. Cosmochim. Acta* **77**, 432–443.

Tesoriero A. J. and Pankow J. F. (1996) Solid solution partitioning of Sr^{2+}, Ba^{2+}, and Cd^{2+} to calcite. *Geochim. Cosmochim. Acta* **60**, 1053–1063.

Toyofuku T., Matsuo M. Y., De Nooijer L. J., Nagai Y., Kawada S., Fujita K., Reichart G.-J., Nomaki H., Tsuchiya M., Sakaguchi H. and Kitazato H. (2017) Proton pumping accompanies calcification in foraminifera. *Nat. Commun.* **8**, 14145.

Towe K. M. and Cifelli R. (1967) Wall ultrastructure in the calcareous foraminifera: crystallographicaspects and a model for calcification. *J. Paleontol.* **41**, 742–762.

Tyszka J., Bickmeyer U., Raitzsch M., Bijma J., Kaczmarek K., Mewes A., Topa P. and Janse M. (2019) Form and function of F-actin during biomineralization revealed from live experiments on foraminifera. *Proc. Natl. Acad. Sci. USA* **116**, 4111–4116.

Urey H. C., Lowenstam H. A., Epstein S. and McKinney C. R. (1951) Measurement of paleotemperatures and temperatures of the upper cretaceous of England, Denmark, and the Southeastern United-States. *Geol. Soc. Am. Bull.* **62**, 399–1000.

Van Dijk I., De Nooijer L. J. and Reichart G. J. (2017a) Trends in element incorporation in hyaline and porcelaneous foraminifera as a function of pCO$_2$. *Biogeosciences* **14**, 497.

Van Dijk I., De Nooijer L. J., Boer W. and Reichart G. J. (2017b) Sulfur in foraminiferal calcite as a potential proxy for seawater carbonate ion concentration. *Earth Planet. Sci. Lett.* **470**, 64–72.

Wetmore K. (1999) Chamber formation in *Archaias angulatus. J. Foraminifer. Res.* **29**, 69–74.

Wit J. C., De Nooijer L. J., Wolthers M. and Reichart G. J. (2013) A novel salinity proxy based on Na incorporation into foraminiferal calcite. *Biogeosciences* **10**, 6375–6387.

Zeebe R. E. and Sanyal A. (2002) Comparison of two potential strategies of planktonic foraminifera for house building: Mg^{2+} or H^+ removal? *Geochim. Cosmochim. Acta* **66**, 1159–1169.

Zeebe R. E. and Westbroek P. (2003) A simple model for the $CaCO_3$ saturation state of the ocean: The "Strangelove", the "Neritan", and the "Cretan" Ocean. *Geochem. Geophys. Geosyst.* **4**.

Associate editor: Anders Meibom